Growth and instability of a laminar plume in a strongly stratified environment

M. LOMBARDI[1], C. P. CAULFIELD[1,2], C. COSSU[3], A. I. PESCI[2] AND R. E. GOLDSTEIN[2]†

[1]BP Institute, University of Cambridge, Madingley Rise, Madingley Road, Cambridge CB3 0EZ, UK

[2]Department of Applied Mathematics & Theoretical Physics, Centre for Mathematical Sciences, University of Cambridge, Wilberforce Road, Cambridge CB3 0WA, UK

[3]IMFT, 1 Allée du Pr. Camille Soula, 31400 Toulouse, France

Experimental studies of laminar plumes descending under gravity into stably stratified environments have shown the existence of a critical injection velocity beyond which the plume exhibits a bifurcation to a coiling instability in three dimensions or a sinuous instability in a Hele-Shaw flow. In addition, flow visualization has shown that, prior to the onset of the instability, a stable base flow is established in which the plume penetrates to a depth significantly smaller than the neutral buoyancy depth. Moreover, the fresh water that is viscously entrained by the plume recirculates within a 'conduit' whose boundary with the background stratification appears sharp. Beyond the bifurcation, the buckling plume takes the form of a travelling wave of varying amplitude, confined within the conduit, which disappears at the penetration depth. To determine the mechanisms underlying these complex phenomena, which take place at a strikingly low Reynolds number but a high Schmidt number, we study here a two-dimensional arrangement, as it is perhaps the simplest system which possesses all the key experimental features. Through a combination of numerical and analytical approaches, a scaling law is found for the plume's penetration depth within the base flow (i.e. the flow where the instability is either absent or artificially suppressed), and the horizontal cross-stream velocity and concentration profile outside the plume are determined from an asymptotic analysis of a simplified model. Direct numerical simulations show that, with increasing flow rate, a sinuous global mode is destabilized giving rise to the self-sustained oscillations as in the experiment. The sinuous instability is shown to be a consequence of the baroclinic generation of vorticity, due to the strong horizontal gradients at the edge of the conduit, a mechanism that is relevant even at very low Reynolds numbers. Despite the strength of this instability, the penetration depth is not significantly affected by it, instead being determined by the properties of the plume in the vicinity of the source. This scenario is confirmed by a local stability analysis. A finite region of local absolute instability is found near the source for sinuous modes prior to the onset of the global instability. Sufficiently far from the source the flow is locally stable. Near the onset of the global instability, varicose modes are also found to be locally, but only convectively, unstable.

Key words: plumes/thermals, stratified flows

† Email address for correspondence: r.e.goldstein@damtp.cam.ac.uk

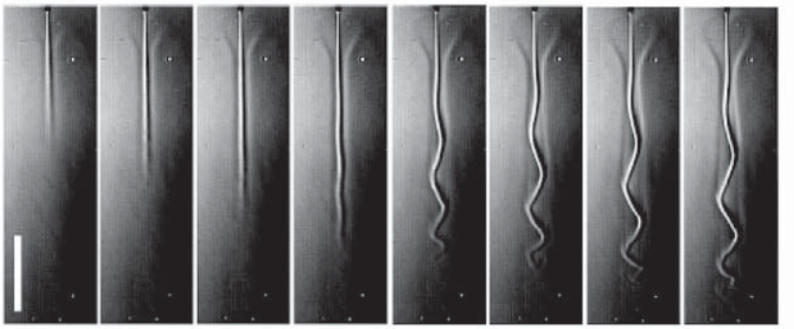

FIGURE 1. Descent of a saline jet into a salinity gradient. Schlieren images at injection rates from 0.02 to 0.18 cm s^{-1} into a gradient with a buoyancy frequency $N = 1.5$ s^{-1}. The scale bar is 1 cm. Image adapted from Pesci, Porter & Goldstein (2003).

1. Introduction

Experimental progress in geophysical, biophysical and environmental fluid dynamics has brought to light a number of situations in which laminar plumes play a central role. These range from the descending plumes of algae-rich fluid in bioconvecting suspensions (Kessler 1985, 1986) and chemosensing by crustaceans (Weissburg & Zimmer-Faust 1994) to magma transport (Helfrich & Whitehead 1990; Hill *et al.* 1992), chimneys in directional solidification (Katz & Worster 2008; Peppin, Huppert & Worster 2008) and chemical precipitation (Cartwright *et al.* 2002; Thouvenel-Romans & Steinbock 2003; Stone & Goldstein 2004; Thouvenel-Romans, van Saarloos & Steinbock 2004; Stone *et al.* 2005). While great effort has been focused on *turbulent* plumes, influenced heavily by the classic work of Morton, Taylor & Turner (1956), surprisingly little attention has been devoted to the rich and complex behaviour that can be displayed by their laminar cousins.

The phenomena explored in some recent experiments involve plumes moving through density-stratified surroundings, a situation of considerable theoretical interest in its own right, for not only is the simplifying hypothesis of self-similarity often inapplicable (Batchelor 1954), but, also, novel types of instabilities occur. For example, a laminar plume descending through a linearly stratified environment exhibits a helical instability beyond a critical flow speed (Dombrowski *et al.* 2005). This instability is fundamentally distinct from the coiling of viscous threads of fluid in air (Ribe 2004), where the surrounding air plays a passive role, and the flickering of a candle (Maxworthy 1999), in which no surrounding stratification is required. Instead, the coiling viscous plume is surrounded by a complicated flow of entrained, recirculating fluid that determines its dynamics. As shown in figure 1, experiments in Hele-Shaw flow (Pesci *et al.* 2003) revealed a quasi-two-dimensional counterpart of the coiling in the form of a sinuous instability of the plume. The conduit edge in the figure encloses the region within which recirculation occurs and is the envelope of the sinuous plume beyond the instability. The plume and the conduit display varicose instabilities near the nozzle, each convected by the local flow.

In these experiments, the typical plume velocity is $u \sim 1$–$5\,\mathrm{mm\,s^{-1}}$, with a source diameter $d \sim 0.5\,\mathrm{mm}$ and a kinematic viscosity $\nu \sim 0.01\,\mathrm{cm^2\,s^{-1}}$, which yields a Reynolds number $Re = ud/\nu \sim 1$. At this Re a plume descending into an *unstratified* medium would be stable. We shall see that instabilities develop as a consequence

of the descent of the plume through stratified surroundings with low diffusivity κ of the solute, i.e. with a large Schmidt number $Sc = \nu/\kappa$ (e.g. $Sc \simeq 700$ in figure 1).

Earlier works (Pesci *et al.* 2003; Dombrowski *et al.* 2005) and recent numerical studies (Schofield & Restrepo 2010) suggested that the coiling instability is driven fully by shear, a hypothesis that reproduces some observed features, but not the flow division into two distinct regions separated by a thin interface (conduit edge), the recirculation pattern of the conduit fluid, the penetration length of the plume and the absolute/convective nature of the instabilities. We show here through direct numerical simulation (DNS), scaling arguments and simplified analytic models that all of the phenomena listed above derive ultimately from a process of 'flux expulsion' which creates the sharp conduit and that the previously ignored baroclinic torques that arise from these gradients produce the instabilities.

This paper is divided into two main parts: (i) analysis of the base flow and the global properties of the plume and (ii) identification of the mechanism and development of the instabilities. The base flow is obtained from two-dimensional DNS. Since the plume is injected continuously into a domain of constant volume, raising the water level, there is no true steady state, and the mean salinity tends asymptotically to that of the plume. In experiments, this problem is mitigated by using a tank with a filling time much longer than that of the plume dynamics, while computationally we utilize positive fluxes of water and momentum through the boundaries of the domain to produce an equivalent ambient distribution. The stability analysis of the quasi-steady state follows a classical procedure, analogous to that applied to the flow on a circular cylinder to explain the oscillations in its wake. First, numerical simulations of the non-parallel problem are performed with small initial perturbations to the symmetric base flow in order to determine the unstable regime. We study the energy equation governing perturbations to gain insight into the instability mechanism and conduct a local stability analysis to reveal the origin and features of the global mode and the competition between absolute and convective instabilities in various parts of the plume (Huerre 2001; Chomaz 2005). In § 2 we discuss the mathematical structure of the problem, the rescaling of the equations of motion and the relevant regime of the non-dimensional parameters. The dynamics of perturbations to the base flow are formulated along with the energetic and local stability analyses. Analysis of the base flow is given in § 3, including a scaling law for the penetration depth of the plume, while in § 4 a simplified model is presented for the generation of the freshwater conduit. In § 5, we discuss the instability at finite amplitude within the DNS and identify the key feature to be strong horizontal gradients in density, which lead to strong generation of baroclinic vorticity through buoyant forcing and expulsion of salt from the central region of the conduit. This expulsion is not unlike the expulsion of magnetic flux by eddies (Weiss 1966; Moffatt 1978) and of passive scalars from convection cells (Shraiman 1987). Because of the very low diffusivity of the stratifying agent (salt), the sinuous instability grows significantly before the strong horizontal density gradients can diffuse away. This holds even when the diffusion of momentum, due to viscosity, is very rapid. We also present a detailed locally parallel (linear) stability analysis demonstrating that while the varicose instability appears always to be convective, and thus will ultimately be advected out of the fluid domain, the sinuous instability is absolute, thus explaining why the latter is the dominant mode observed in experiments. We establish that the instability has little effect on the penetration depth of the plume. The concluding section, § 6, offers suggestions for extensions to this work and for future experiments.

2. Mathematical formulation

We consider the physical set-up used in the relevant experiments (Pesci *et al.* 2003). Fluid of constant density ρ_i enters our domain through a source of width d, centred at the origin. Choosing the vertical, along-stream coordinate z to increase downwards, the ambient fluid has (constant) density ρ_0 at $z=0$ and has a linear statically stable density gradient such that at height $z=H$ (typically the base of the experimental tank) $\rho=\rho_i$. It is then convenient to decompose the density field into a linear background part, which is constant in time, and a time-dependent deviation,

$$\rho = \rho_0 + \frac{(\rho_i - \rho_0)z}{H} + \rho' = \overline{\rho}(z) + \rho'. \tag{2.1}$$

Although ρ' would typically be referred to as a 'perturbation', we refer to it as a 'deviation' from the background profile, since it is possible for a quasi-steady non-parallel and non-hydrostatic laminar 'base plume' of *finite* extent to develop in the flow. Lateral diffusion of salt out from the plume causes its length to be much smaller than the depth at which the ambient density matches that of the fluid at the source. Using (2.1), we identify the non-hydrostatic component $p'(x,z,t)$ of the pressure as

$$p = p'(x,z,t) + \overline{p}(z), \quad \frac{\mathrm{d}\overline{p}}{\mathrm{d}z} = g\overline{\rho}. \tag{2.2}$$

We apply the Boussinesq approximation with ρ_0 as the reference density. Defining $g' = g\rho'/\rho_0$ as the deviation reduced gravity, where g is the gravitational acceleration, the two-dimensional Navier–Stokes equations and that of mass conservation become

$$\frac{\partial \boldsymbol{u}}{\partial t} + \boldsymbol{u}\cdot\nabla\boldsymbol{u} = -\frac{1}{\rho_0}\nabla p' + g'\hat{\boldsymbol{k}} + \nu\nabla^2\boldsymbol{u}, \tag{2.3a}$$

$$\frac{\partial g'}{\partial t} + \boldsymbol{u}\cdot\nabla g' = \kappa\nabla^2 g' - N^2 w, \tag{2.3b}$$

$$\nabla\cdot\boldsymbol{u} = 0, \tag{2.3c}$$

where $\hat{\boldsymbol{k}}$ is the unit vector in the z-direction, and the velocity $\boldsymbol{u}=(u(x,z,t), w(x,z,t))$ and $\rho'(x,z,t)$ depend on time, z and the horizontal (cross-stream) direction x. The only appearance of the background density gradient is as a forcing of the deviation reduced gravity g' scaled by the background buoyancy frequency N^2. If $g'_i = g(\rho_i - \rho_0)/\rho_0$ is the reduced gravity of the fluid entering the plume from the source, then

$$N^2 = \frac{g'_i}{H}, \quad G' = g' + N^2 z, \tag{2.4}$$

defining the total reduced gravity G'. We take the curl of (2.3) to obtain the equation of motion of the vorticity $\boldsymbol{\Omega} = \Omega\,\hat{\boldsymbol{j}}$,

$$\frac{\partial \Omega}{\partial t} + \boldsymbol{u}\cdot\nabla\Omega = -\frac{\partial g'}{\partial x} + \nu\nabla^2\Omega, \quad \text{where} \quad \Omega = \frac{\partial u}{\partial z} - \frac{\partial w}{\partial x}\ . \tag{2.5}$$

The structure of (2.5) shows a crucial feature; because of the non-uniform density distribution, even in two dimensions not only is the vorticity advected and diffused, but it can be created or destroyed by *horizontal* gradients in density. This is the Boussinesq *baroclinic torque* produced by misalignment of pressure and density isosurfaces. As we shall see, this baroclinic term plays the central role in the development of flow instabilities.

We choose to non-dimensionalize the quantities in terms of the source width d and the viscous time scale d^2/ν and follow the convention that non-dimensional dependent

variables have carets, while non-dimensional independent variables are (lower-case) greek. Hence,

$$\boldsymbol{u} = \frac{\nu}{d}\hat{\boldsymbol{u}}, \quad \frac{p'}{\rho_0} = \frac{\nu^2}{d^2}\hat{p}, \quad g' = \frac{\nu^2}{d^3}\hat{g}, \quad \Omega = \frac{\nu}{d^2}\hat{\Omega}, \tag{2.6a}$$

$$t = \frac{d^2}{\nu}\tau, \quad x = d\xi, \quad z = d\zeta, \quad N^2 = \frac{\nu^2}{d^4}\hat{N}^2, \quad \hat{G} = \hat{g} + \hat{N}^2\zeta. \tag{2.6b}$$

Thus, $\hat{N}$ is the ratio of the background buoyancy time scale to a diffusive time. Using these scalings, the governing equations (2.3) and (2.5) become

$$\frac{\partial \hat{\boldsymbol{u}}}{\partial \tau} + \hat{\boldsymbol{u}} \cdot \nabla \hat{\boldsymbol{u}} = -\nabla \hat{p} + \hat{g}\hat{\boldsymbol{k}} + \nabla^2 \hat{\boldsymbol{u}}, \tag{2.7a}$$

$$\frac{\partial \hat{\Omega}}{\partial \tau} + \hat{\boldsymbol{u}} \cdot \nabla \hat{\Omega} = -\frac{\partial \hat{g}}{\partial \xi} + \nabla^2 \hat{\Omega}, \tag{2.7b}$$

$$\frac{\partial \hat{g}}{\partial \tau} + \hat{\boldsymbol{u}} \cdot \nabla \hat{g} = \frac{1}{Sc}\hat{\nabla}^2 \hat{g} - \hat{N}^2 \hat{w}, \tag{2.7c}$$

where the gradient operator is now with respect to rescaled variables, i.e. $\nabla = (\partial/\partial\xi, \partial/\partial\zeta)^T$.

As the midpoint of the fluid source is located at the origin, the boundary conditions on the deviation reduced gravity are $\hat{g}(\xi, 0, \tau) = Gr$ for $|\xi| < 1/2$ and $\hat{g} = 0$ elsewhere, with $\hat{g}(\xi, \zeta, \tau) \to 0$ as $|\xi| \to \infty$ for $\zeta > 0$, where Gr is the Grashof number,

$$Gr = \frac{g_i' d^3}{\nu^2}. \tag{2.8}$$

The horizontal velocity $\hat{u}$ has boundary conditions $\hat{u}(\xi, 0, \tau) = 0$, and $\hat{u}(\xi, \zeta, \tau) \to 0$ as $|\xi| \to \infty$ for $\zeta > 0$. The source volume flux Q_i defines the Reynolds and Péclet numbers,

$$Re = \frac{Q_i}{\nu}, \quad Pe = Re\frac{\nu}{\kappa}. \tag{2.9}$$

In the simplest case of constant velocity across the source before entrance into the flow domain, the appropriate boundary condition is $\hat{w}(\xi, 0, \tau) = Re$ for $|\xi| < 1/2$ and zero elsewhere, with $\hat{w}(\xi, \zeta) \to 0$ as $|\xi| \to \infty$ for $\zeta > 0$. It is now clear that there are four non-dimensional parameters that govern the flow; the Schmidt number Sc and the scaled buoyancy frequency $\hat{N}$ are determined by the properties of the experimental fluid and appear in the governing equations (2.7), while the Grashof number Gr and the Reynolds number Re are properties of the input plume and appear in the boundary conditions. From (2.7c), since the Schmidt number is very large in the flows we are considering, there is little diffusion of the reduced gravity, and therefore non-trivial baroclinic vorticity generation is possible, even though the Reynolds number is small, and hence momentum is rapidly diffused. Moreover, the only role of the background density gradient is to determine the coupling between the deviation reduced gravity $\hat{g}$ and the vertical velocity through $\hat{N}^2$.

2.1. *Perturbation equations*

We now decompose the velocity and reduced gravity deviations into a steady part satisfying the time-independent version of (2.7) and a time-dependent perturbation,

$$\hat{\boldsymbol{u}}(\xi, \zeta, \tau) = \boldsymbol{u}_S(\xi, \zeta) + \tilde{\boldsymbol{u}}(\xi, \zeta, \tau), \tag{2.10a}$$

$$\hat{g}(\xi, \zeta, \tau) = g_S(\xi, \zeta) + \tilde{g}(\xi, \zeta, \tau), \tag{2.10b}$$

$$\hat{p}(\xi, \zeta, \tau) = p_S(\xi, \zeta) + \tilde{p}(\xi, \zeta, \tau), \tag{2.10c}$$

$$\hat{\Omega}(\xi, \zeta, \tau) = \Omega_S(\xi, \zeta) + \tilde{\Omega}(\xi, \zeta, \tau). \tag{2.10d}$$

Under the further assumption that the perturbation is small in amplitude relative to the steady flow, we linearize about this flow and find (with $\nabla \cdot \tilde{\boldsymbol{u}} = 0$)

$$\frac{\partial \tilde{\boldsymbol{u}}}{\partial \tau} + \boldsymbol{u}_S \cdot \nabla \tilde{\boldsymbol{u}} + \tilde{\boldsymbol{u}} \cdot \nabla \boldsymbol{u}_S = -\nabla \tilde{p} + \tilde{g}\hat{\boldsymbol{k}} + \nabla^2 \tilde{\boldsymbol{u}}, \tag{2.11a}$$

$$\frac{\partial \tilde{\Omega}}{\partial \tau} + \boldsymbol{u}_S \cdot \nabla \tilde{\Omega} + \tilde{\boldsymbol{u}} \cdot \nabla \Omega_S = -\frac{\partial \tilde{g}}{\partial \xi} + \nabla^2 \tilde{\Omega}, \tag{2.11b}$$

$$\frac{\partial \tilde{g}}{\partial \tau} + \boldsymbol{u}_S \cdot \nabla \tilde{g} + \tilde{\boldsymbol{u}} \cdot \nabla g_S = \frac{1}{Sc} \nabla^2 \tilde{g} - \hat{N}^2 \tilde{w}. \tag{2.11c}$$

2.2. *Energetics of the perturbation*

Further insight into the physical mechanisms can be obtained from the evolution equation for the kinetic energy of perturbations, which is found by taking the dot product of (2.11*a*) with $\tilde{\boldsymbol{u}}$ and integrating over the domain $\mathscr{D}$. We assume that the lateral and lower boundaries are far enough from the source so that the normal components of all velocities vanish and hence do not contribute to the integral. However, there are contributions from the source at the upper boundary ($\zeta = 0$). We define the perturbation kinetic energy density $\mathscr{K} = \langle |\tilde{\boldsymbol{u}}|^2/2 \rangle$, where the spatial averaging operator $\langle \phi(\xi, \zeta) \rangle$ is given by

$$\langle \phi(\xi, \zeta) \rangle = \lim_{\xi_{\mathscr{D}}, \zeta_{\mathscr{D}} \to \infty} \frac{1}{\xi_{\mathscr{D}} \zeta_{\mathscr{D}}} \int_{-\xi_{\mathscr{D}}/2}^{\xi_{\mathscr{D}}/2} \int_0^{\zeta_{\mathscr{D}}} \phi(\xi, \zeta) \, \mathrm{d}\zeta \, \mathrm{d}\xi, \tag{2.12}$$

for some variable ϕ. The evolution equation for $\mathscr{K}$ is

$$\frac{\mathrm{d}\mathscr{K}}{\mathrm{d}\tau} = \mathscr{I} - \mathscr{S} + \langle \tilde{g}\tilde{w} \rangle, \tag{2.13}$$

where

$$\mathscr{I} = \left\langle (\tilde{u}^2 - \tilde{w}^2) \frac{\partial w_S}{\partial \zeta} \right\rangle - \left\langle \tilde{u}\tilde{w} \left(\frac{\partial w_S}{\partial \xi} + \frac{\partial u_S}{\partial \zeta} \right) \right\rangle - \langle \|\nabla \tilde{\boldsymbol{u}}\|^2 \rangle, \tag{2.14a}$$

$$\mathscr{S} = \int_{-1/2}^{1/2} \left(w_S \frac{|\tilde{\boldsymbol{u}}|^2}{2} - \tilde{p}\tilde{w} + \frac{\partial}{\partial \zeta} \left[\frac{|\tilde{\boldsymbol{u}}|^2}{2} \right] \right) \mathrm{d}\xi \Bigg|_{\zeta = 0} \tag{2.14b}$$

and

$$\|\nabla \tilde{\boldsymbol{u}}\|^2 = \left(\frac{\partial}{\partial \xi} \tilde{u} \right)^2 + \left(\frac{\partial}{\partial \zeta} \tilde{u} \right)^2 + \left(\frac{\partial}{\partial \xi} \tilde{w} \right)^2 + \left(\frac{\partial}{\partial \zeta} \tilde{w} \right)^2. \tag{2.14c}$$

In (2.13), $\mathscr{I}$ is a contribution from the velocity within the interior of the domain, which may drive an increase in $\mathscr{K}$ due to inertial effects (anisotropic strain or Reynolds stresses) or a decrease due to viscous dissipation. Since we consider small Re, we expect the latter to dominate, and thus, the classical mechanisms for inertial forcing of an instability are not present. The term $\mathscr{S}$ is the boundary forcing by the base flow, pressure and diffusion. As we shall see, typical unstable perturbations have exceedingly small $\mathscr{S}$ values. The remaining term $\langle \tilde{g}\tilde{w} \rangle$, a buoyancy flux, is sufficiently positive to be the driving force behind the instabilities. This and the baroclinic term in (2.7*b*) play equivalent roles in capturing the effect of non-uniformity in the density distribution.

2.3. *Spatio-temporal local stability analysis*

The flow described by (2.11) reproduces the instabilities observed experimentally and allows us to determine the nature of the global instability (Chomaz 2005) by analysing the local stability properties of a notional parallel base flow ($u_S^\zeta = 0$) that depends only on ξ and is defined by the steady velocity and density distributions at some position ζ_S:

$$\boldsymbol{u}_S^\zeta(\xi) = (0, w_S(\xi, \zeta_S))^T, \quad g_S^\zeta(\xi) = g_S(\xi, \zeta_S), \tag{2.15}$$

where g_S^ζ is defined in terms of the deviation from the steady linear gradient in density.

Since the variations with ζ_S of both the base flow and the concentration profile are weak, and the vertical velocity w_S of the steady-state plume at typical heights is substantially larger than the cross-stream velocity u_S, this local analysis is justified. Moreover, the presence of the background gradient does not violate this assumption because, from (2.7), it acts simply as a forcing on the deviation reduced gravity and does not play any other role provided the hydrostatic component of the pressure is removed. Assuming further that the perturbations $\tilde{\boldsymbol{u}}(\xi, \zeta)$ and $\tilde{g}(\xi, \zeta)$ away from this parallel flow are relatively small, their evolution equations are only slightly different from (2.11) and are given by

$$\frac{\partial \tilde{\boldsymbol{u}}}{\partial \tau} + w_S^\zeta \frac{\partial \tilde{\boldsymbol{u}}}{\partial \zeta} + \tilde{u} \frac{\mathrm{d}w_S^\zeta}{\mathrm{d}\xi} \hat{\boldsymbol{k}} = -\nabla \tilde{p} + \tilde{g} \hat{\boldsymbol{k}} + \nabla^2 \tilde{\boldsymbol{u}}, \tag{2.16a}$$

$$\frac{\partial \tilde{g}}{\partial \tau} + w_S^\zeta \frac{\partial \tilde{g}}{\partial \zeta} + \tilde{u} \frac{\mathrm{d}g_S^\zeta}{\mathrm{d}\xi} = \frac{1}{Sc} \nabla^2 \tilde{g} - \hat{N}^2 \tilde{w}. \tag{2.16b}$$

As usual, the stability properties of the basic parallel flow are revealed by use of a Green's function, the linear evolution of an impulsive initial condition, as $\tau \to \infty$. When the amplitude of the impulse response tends to zero the flow is stable. On the other hand, when the Green's function grows as $\tau \to \infty$ but tends to zero at the position $\boldsymbol{\zeta}_0$ of the initial pulse, then the instability is said to be *convective*. Otherwise, it is *absolute*. An impulse in a convectively unstable flow is therefore amplified while being advected downstream, whereas it is able to grow in place in an absolutely unstable flow.

Here, the local stability properties are determined by analysis of the impulse response obtained by DNS following a standard technique (Delbende & Chomaz 1998; Delbende, Chomaz & Huerre 1998; Brandt *et al.* 2003). We assume that a typical perturbation variable $\tilde{\phi}(\xi, \zeta, \tau)$ (where $\tilde{\phi}$ could be a velocity component, for example) is oscillatory in the ζ-direction and define its wave amplitude by introducing the analytical complex field $\phi_c(\xi, \zeta, \tau)$ that can be obtained through a Hilbert transform in such a way that the field $\tilde{\phi}$ is the real part of ϕ_c (Delbende & Chomaz 1998; Delbende *et al.* 1998; Brandt *et al.* 2003). The spatio-temporal amplitude $\Phi(\zeta, \tau)$ of the variable $\tilde{\phi}(\xi, \zeta, \tau)$ is then defined by

$$\Phi(\zeta, \tau) = \left(\frac{1}{\xi_{\mathscr{D}}} \int_{-\xi_{\mathscr{D}}/2}^{\xi_{\mathscr{D}}/2} |\phi_c(\xi, \zeta, \tau)|^2 \, \mathrm{d}\xi \right)^{1/2}, \tag{2.17}$$

where $\xi_{\mathscr{D}}$ is the horizontal extent of the flow domain.

It can be shown (Huerre 2001) that the temporal growth rate σ observed while travelling at the group velocity v_g can be evaluated for large τ from Φ in (2.17) as

$$\sigma(v_g) \sim \frac{\partial}{\partial \tau} \ln[\tau^{1/2} \Phi(\zeta_0 + v_g \tau, \tau)]. \tag{2.18}$$

For unstable flows, $\sigma > 0$ for some range of v_g. In usual situations the Green response consists of a single wavepacket with leading- and trailing-edge velocities v_g^+ and v_g^- respectively defined by $\sigma(v_g^-) = \sigma(v_g^+) = 0$. In the case of an absolutely unstable base flow the two fronts travel in opposite directions, and the wavepacket amplitude grows in the position of the initial pulse ($\sigma(v_g = 0) > 0$). In the convectively unstable case $\sigma(v_g = 0) < 0$, and the two fronts travel in the same direction.

2.4. *Numerical formulation*

The numerical scheme consists of a spectral element method whose accuracy is essential to resolve the high cross-stream gradients near the source. For the velocity and concentration fields we used elements of degree 14 in the cross-stream direction and degree 6 in the downstream direction. In order to satisfy the *inf–sup* condition which prevents the formation of spurious modes in the pressure field, the elements used for the pressure have to be two orders lower than those for the velocity (Auteri, Guermond & Parolini 2001). We solved the ensuing linear system at each time step by using the highly efficient UMFPACK package (Davis & Duff 1997). The time discretization was based on an implicit Euler scheme, where the nonlinear advective terms are approximated semi-implicitly, and the deviation reduced gravity term in (2.7) is in explicit form,

$$\frac{\hat{\boldsymbol{u}}^{n+1} - \hat{\boldsymbol{u}}^n}{\Delta\tau} + \hat{\boldsymbol{u}}^n \cdot \nabla\hat{\boldsymbol{u}}^{n+1} = -\nabla\hat{p}^{n+1} + \hat{g}^n\hat{\boldsymbol{k}} + \nabla^2\boldsymbol{u}^{n+1}, \tag{2.19a}$$

$$\frac{\hat{g}^{n+1} - \hat{g}^n}{\Delta\tau} + \boldsymbol{u}^n \cdot \nabla\hat{g}^{n+1} = \frac{1}{Sc}\nabla^2\hat{g}^{n+1} - \hat{N}^2\hat{w}^n, \tag{2.19b}$$

where $\hat{\boldsymbol{u}}^n = (\hat{u}^n, \hat{w}^n)$ is the velocity field at the nth time step $\tau_n = \tau_0 + n\Delta\tau$. Though this method utilizes a first-order time stepping, this does not compromise the accuracy, since the high Schmidt number requires the use of an extremely small time step $\Delta\tau$.

Convergence tests were conducted to verify the DNS accuracy (Lombardi 2008). To reduce the computational burden, and since the penetration depth is substantially less than H, we limited the domain size to twice the penetration depth. We also imposed a rigid upper boundary condition. The source conditions of reduced gravity and vertical velocity were continuous, with constant values for $|\xi| < 1/2$ and edges dropping to zero continuously modelled by half a Gaussian with very small standard deviation and an inflection point located at $\xi = \pm 1/2$. The velocity was scaled to be Re so that the total downward flux was the required value, while the reduced gravity was set to Gr within the 'source' region $|\xi| < 1/2$. Symmetric lateral boundaries were chosen so that the overall domain width was large enough to avoid any interaction of the boundaries with the plume. Neumann conditions were chosen for the deviation reduced gravity and velocity at the bottom boundary, thus permitting flux through the boundary to balance the inlet flux, and therefore the background density gradient exhibited negligible variation during a simulation.

For sufficiently small volume fluxes from the source, the 'base plume' was stable to small perturbations and was computed by DNS with the source of plume fluid switched on at $\tau = 0$ and flowing into an initial linear density gradient. The resulting transient decays quickly, and the solution rapidly converges to the quasi-steady symmetric base plume. It was also possible to compute the base plume in the linearly unstable domain by a continuation method. Because of the high precision and grid symmetry of the numerical scheme and of the initial conditions it was not necessary to enforce explicitly the symmetry. Once the base flow converged to a steady state,

Parameter	Symbol	Reference value
Source diameter	d	$d_r = 0.05$ cm
Source reduced gravity	g_i'	$g_r' = 39.2$ cm s^{-2}
(Dimensional) buoyancy frequency	N^2	$N_r^2 = 1.56$ s^{-2}
Diffusivity of salt	κ	1.5×10^{-5} cm^2 s^{-1}
Kinematic viscosity of water	ν	0.01 cm^2 s^{-1}
Schmidt number ν/κ	σ	667
Grashof number $g_i' d^3/\nu^2$	Gr	49.05
Non-dimensional buoyancy frequency	$\hat{N}^2$	9.75×10^{-2}
Reynolds number Q/ν	Re	0.05

TABLE 1. Experimental parameters chosen as the reference case.

its stability was investigated by adding low-amplitude asymmetric noise to both the velocity and concentration fields at the source.

The local stability of the flow defined by both w_S^ζ and g_S^ζ was analysed by discretizing (2.16) and using the same approach as for (2.19) with periodic boundary conditions at the top and bottom of the domain. To build a numerical approximation for the Green's function of the flow the delta-function forcing was approximated by a highly localized initial perturbation of the stream function $\tilde{\psi}(\xi, \zeta)$ near a reference location ξ_0, ζ_0:

$$\tilde{\psi}(\xi, \zeta) = A_\epsilon \exp(-\bar{\xi}^2 - \bar{\zeta}^2), \tag{2.20}$$

where $\bar{\xi} = (\xi - \xi_0)/\lambda_\xi$ and $\bar{\zeta} = (\zeta - \zeta_0)/\lambda_\zeta$ and λ_ξ and λ_ζ are some spatial reference lengths, small enough so that the perturbation is highly localized but large enough to be adequately resolved by the grid spacing. Typically, we found that choosing λ_ξ and λ_ζ to be the same order as the plume diameter worked well.

We chose the centre of the impulse (ξ_0, ζ_0) to be in the upper part of the domain, slightly offset horizontally from the plane of symmetry of the velocity and concentration, to ensure that the antisymmetric modes were the ones excited. From (2.20) the horizontal and vertical velocity impulses are $(\tilde{u}, \tilde{w}) = (\partial\tilde{\psi}/\partial\zeta, -\partial\tilde{\psi}/\partial\xi)$, while the concentration impulse was chosen to be proportional to $\tilde{\psi}$. The wavepacket amplitudes were found by post-processing perturbation fields at selected times. The amplitude $\Phi(\zeta - \zeta_0, \tau)$ for these various fields was computed by interpolating the perturbation fields on a regular grid and then applying the discrete Hilbert transform based on a fast Fourier transform in the ζ-periodic direction and then by quadrature in the ξ-direction.

3. Base plume flow analysis

3.1. *Flow structure*

We use the experiments of Pesci *et al.* (2003) as a reference for the material parameters listed in table 1. Figure 2 shows two of the main fields, the non-dimensional total reduced gravity $\hat{G}$ and the vorticity $\hat{\Omega}$ as defined in (2.6). The presence of the ambient density gradient greatly modifies the dynamics of the descending plume. There is a finite penetration depth of the plume, much above that at which the ambient fluid has a density equal to the injected plume fluid. Over most of the distance to this penetration depth, there is a very thin conduit surrounding the plume, with extremely strong horizontal density gradients, which lead to very large values of the vorticity. Within this conduit there is substantial vertical velocity which decays in

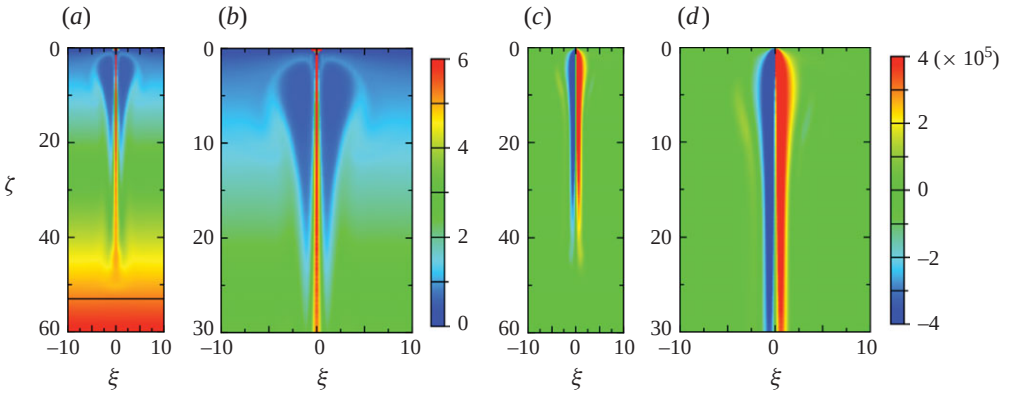

FIGURE 2. The reference base plume flow as defined in table 1. (*a*) Total reduced gravity $\hat{G}$ as defined in (2.6) and (*b*) enlargement of source region. (*c*) Vorticity $\hat{\Omega}$ and (*d*) enlargement. The black line in (*a*) marks the penetration depth.

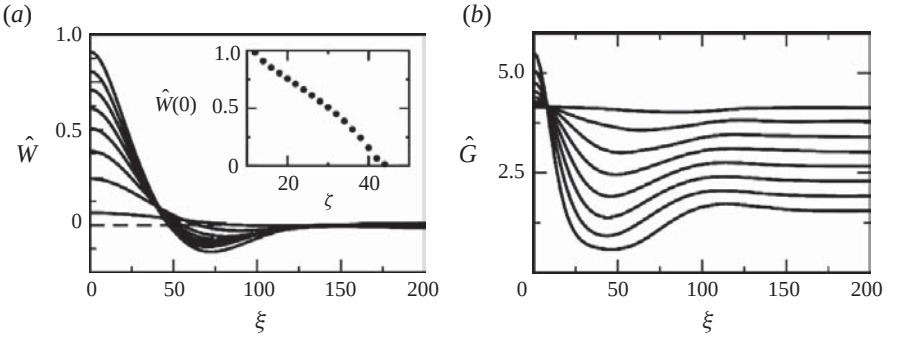

FIGURE 3. Variation of plume properties at equally spaced depths. (*a*) Vertical velocity $\hat{w}$ and (*b*) $\hat{G}$, the total reduced gravity, for the parameters defined in table 1, at $\zeta = 14, 18, 22, \ldots, 42$. The inset of (*a*) shows the downward velocity at the centre of the plume as a function of depth.

both directions. Moreover, there is also a strong recirculation region near the source, characterized by non-trivial horizontal velocities and upward vertical flow, and it is composed principally of fluid whose density is very close to that of the background at the upper surface. Just below the source we find that the plume accelerates and narrows, entraining the ambient fluid that then sets up the recirculation.

The qualitative picture of the numerical simulations is the same for all values of the Reynolds number (even zero). The imposed Dirichlet boundary condition of fixed Gr at the source ensures that the dense fluid always diffuses into the ambient one and then accelerates downwards under the influence of gravity, leading to the development of a descending plume and its recirculation region. Conversely, at the low flow rates in experiments, diffusion at the source would lead to reduced density within the input tube and hence reduce, and perhaps even completely suppress, the flux of the source fluid into the ambient one.

The dynamics of finite penetration depth can be understood by considering horizontal profiles of the vertical velocity $\hat{w}$ and the total reduced gravity $\hat{G}$, as shown in figure 3. The acceleration near the source and the upward vertical flow,

which is a negative velocity in our coordinate system, along with the above observation that a base flow exists even for $Re = 0$, suggest that there is a zone of adjustment for the development of a proper plume-like behaviour and thus that the source value of the Reynolds number does not necessarily capture all the important aspects of the flow development. The total reduced gravity plots also show that the plume viscously entrains fluid from nearer the source and drags it downwards, reinforcing the presence of lower-density fluid in the recirculation region relative to the far-field environment at that location. This acceleration is also essential to the scaling arguments presented below. The plume stops when its density reaches that of the ambient, with no inertial overshooting. The inset of figure 3(*a*) indicates that the central velocity of the plume decreases approximately linearly to zero at the termination depth. Although the density in the ambient does increase with depth, the source density rapidly decreases through diffusion; hence the short penetration depth. The reduced density of the conduit enhances the diffusive loss of solute from the plume.

3.2. *Penetration depth scaling*

While it is clear that changing density offsets and gradients will affect the penetration depth Z_p, the observation that the base plume reaches a finite depth even when the source Reynolds number is zero suggests that Z_p is not a strong function of viscosity. Hence, we hypothesize that Z_p depends on the effective buoyancy flux B_e (per unit width) issuing from the source and the buoyancy frequency in the ambient fluid, where

$$B_e = g_i' w_e d_e, \tag{3.1}$$

where w_e is an effective velocity due to the density difference near the source and d_e is the effective width, which is proportional to d. A key step is to determine an appropriate value for the *macroscopic* velocity near the source even at $Q = 0$. This velocity is set by the boundary condition of fixed Gr at the source. For plumes with $Q = 0$ one expects $w_e \propto g_i'/N$, and therefore the assumption that Z_p depends on B_e (with dimensions L^3T^{-3}) and N (with dimensions T^{-1}) suggests that Z_p is given by

$$Z_p = A\frac{(g_i')^{2/3}d^{1/3}}{N^{4/3}}, \tag{3.2}$$

for some constant A. To test this prediction we varied g_i', d and N^2 for a plume with $Re = 0$ relative to the reference values g_r', d_r and N_r^2 listed in table 1 and determined the scalings by least-squares fitting, as shown in figure 4. The best-fit scalings for the power dependence of the (dimensional) source reduced gravity, the source width and the buoyancy frequency are 0.65, 0.38 and -1.24, with constant of proportionality $A \simeq 0.5$. This evidence strongly suggests that, at least for small source volume fluxes, the assumption of an 'effective' buoyancy flux is appropriate to determine the penetration depth.

The situation is more complicated for flows with $Re \neq 0$, where there is a finite source volume flux. In such cases, the effective buoyancy flux is determined not only by the diffusive process discussed above but also by the actual macroscopic flow being driven through the source. Interestingly, for reasons that are still unclear, the scaling of the penetration depth with ambient buoyancy frequency appears to be independent of the source volume flux, with the penetration depth continuing to be proportional to $N^{-4/3}$. Unsurprisingly, increasing the source volume flux (and hence the exit velocity of the plume fluid) increases the penetration depth of the base plume, though this increase is relatively weak, and there does not appear to be any straightforward power-law dependence.

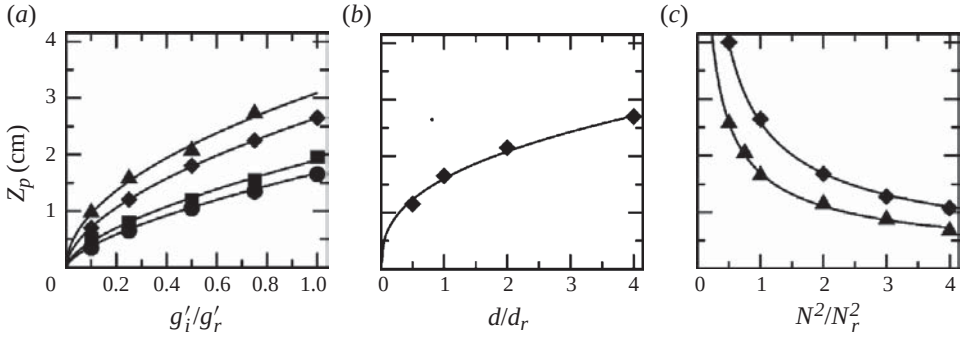

FIGURE 4. Variation of penetration depth with flow parameters, at $Pe = 0$, for (a) relative source reduced gravity g'_i/g'_r, (b) relative source width d/d_r and (c) relative dimensional buoyancy frequency N/N_r, where the reference values are as defined in table 1. Numerical results are marked with the symbols, and the best-fit power laws are shown with the solid lines.

4. Simplified model for the formation of the freshwater conduit

In this section we address the fundamental question of what determines the location and thickness of the conduit edge. We find an answer by means of a simplified model of the large-scale base flow driven by the descending plume. Because the edge is located away from any boundaries, it should be considered an 'internal boundary layer'. This problem is very closely related to one previously studied involving diffusive transport in a Rayleigh–Bénard convection cell (Shraiman 1987), where such a boundary layer has a particular scaling with the Péclet number and is associated with a separatrix in the flow.

As shown in figure 3, the descending plume drives a global circulation in the conduit. If we focus on the flow structure at distances much greater than the width of the plume, an equivalent global flow can be established by a moving wall; although this neglects diffusion and lateral spreading of the plume fluid, it highlights the role of the large-scale circulation in determining the location of the conduit edge and its thickness. Thus, a natural simplified model would consist of a closed volume of linearly stratified fluid, where a wall moves tangentially. The simplest problem of this type, a wall moving with *uniform* tangential velocity at an arbitrary angle to the vertical, was investigated by Standing (1971), who developed a linearized approximation for small perturbations to the background and found a boundary layer adjacent to the wall whose thickness varies as $Sc^{-1/4}$. More recent work (Blanchette, Peacock & Cousin 2008) has addressed the stability of such flows for vertical walls. Here, we consider a vertical 'wall' whose velocity decreases linearly with depth, reaches zero at a finite distance and remains stationary below that point. This boundary condition is motivated by the numerical results (figure 3). Although it is like that of certain well-known stretching-wall problems for which, under certain circumstances, similarity solutions exist (Drazin & Riley 2006), the effect of stretching boundary conditions on stratified flows has barely been studied.

For this simplified problem, it is straightforward to fix the properties of the ambient fluid, and therefore we set the (dimensional) buoyancy frequency N^2 and the kinematic viscosity ν to the values in table 1. Beyond a Schmidt number of $\sim$100 we find no qualitative change in the results, but the computational burden of resolving fine features becomes increasingly onerous. Hence we chose for the simulations $Sc = 200$,

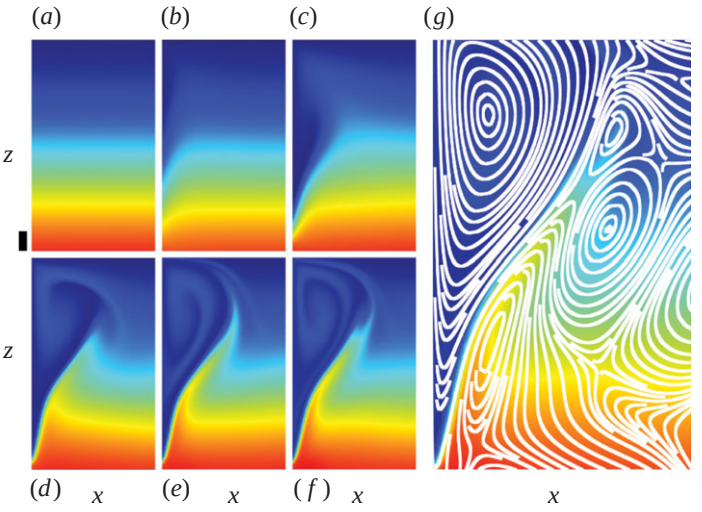

FIGURE 5. Moving-wall simulations. (*a*)–(*f*) Evolution of the total reduced gravity at times $t = 0$, 100, 300, 600, 1000 and 1200 s after the start of the motion. (*g*) As shown by the white streamlines, the conduit of fresh water displays a sharp edge that coincides with the separatrix between the large vortex adjacent to the wall and the remainder of the flow. The scale bar is 2 cm.

which is far beyond the threshold and yet still computationally manageable. The situation with the source conditions is subtler, since having replaced the plume by a moving wall, there is no longer the source width d used in the rescalings (2.6), nor the source reduced gravity g_i'. If a direct comparison with the full problem were desired, it would be possible to find appropriate values of the maximum wall velocity w_w and the distance Z_w over which the velocity drops to zero. Specifically in the case in which $Re = 0$, we can require that w_w corresponds to the effective velocity w_e discussed in § 3.2, thus defining an implicit equivalent value for the source reduced gravity of the notional equivalent plume:

$$w_w = w_e = \frac{g_i'}{N} \rightarrow g_i' = N w_w. \tag{4.1}$$

Similarly, if we require the penetration depth Z_p as defined in (3.2) to match Z_w, we can use (3.2) and (4.1) to define an implicit value for d:

$$Z_w = Z_p = A\frac{(g_i')^{2/3} d^{1/3}}{N^{4/3}} \rightarrow d = \left(\frac{Z_w}{A}\right)^3 \left(\frac{N}{w_w}\right)^2. \tag{4.2}$$

Here, for clarity, we choose to increase Z_w to 10 cm (3–4 times larger than in the full numerics) and set $w_w = 0.1\ \mathrm{cm\,s^{-1}}$, thereby enlarging the extent of the recirculation region. Without the need to resolve fine structure, we used a commercial finite-element code (Comsol).

Figure 5 shows the evolution of the rescaled total reduced gravity G'/g, where G' is defined in (2.4), after the wall begins its motion. Starting from a uniform stratification in the chamber, the moving wall creates a vortical flow – downwards near the wall, upwards far from it – and the vortex spreads laterally until finally saturating at a fixed size. The steady state displays nearly pure water in the circulating conduit and a sharp conduit edge, with a shape very similar to that seen in the full numerics (figure 2*b*). This effect is the salinity counterpart (Rhines & Young 1983) of the expulsion

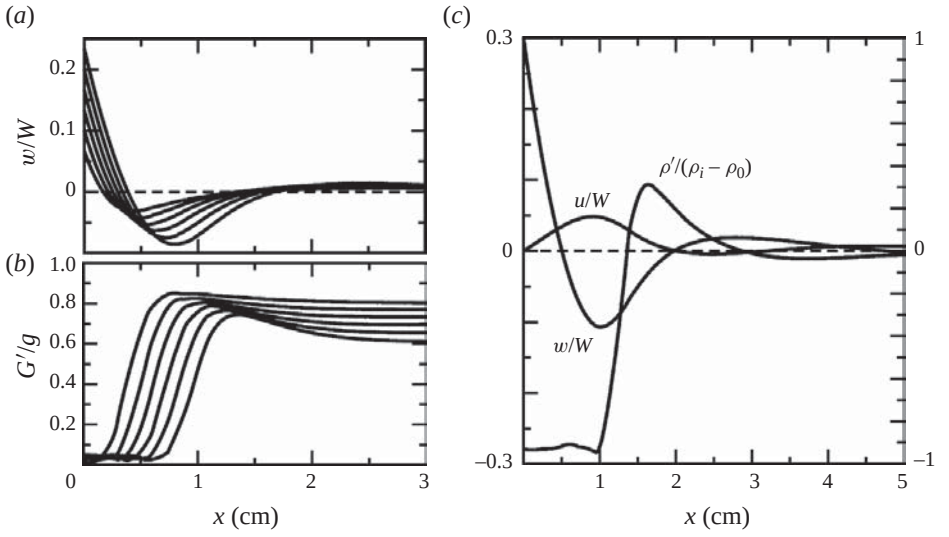

FIGURE 6. Moving-wall simulations. (*a*) Normalized downward fluid velocity and (*b*) rescaled total reduced gravity at various depths. (*c*) The two components of velocity (scale on left axis) and the rescaled density offset (right axis), showing that the sharp front in density occurs away from the point of vanishing velocities and close to the maximum of the vertical velocity.

of magnetic flux by eddies (Weiss 1966; Moffatt 1978), where the relevant scalar is the out-of-plane component of the magnetic vector potential in the regime of large magnetic Reynolds number.

Figures 6(*a*) and 6(*b*) show the downward velocity and G'/g as a function of the lateral distance x from the wall at various depths below the top of the moving wall. These profiles are qualitatively similar to those from the full numerical simulation (figure 3). The key difference between the computations is seen in the concentration profiles, where, naturally, the moving-wall simulation does not display the return of the solute concentration to a local maximum at $\xi = 0$. Figure 6(*c*) shows the fluctuation density field ρ' and the two components of velocity along a cross-section through the conduit at a point one third of the distance up the moving wall. The density exhibits a rapid change from a nearly constant negative value within the conduit through to a positive peak and then a slow, oscillatory decay back to zero as the density field approaches that of the background stratification. The location of the maximum gradient of ρ' is a natural definition of the conduit edge in light of the fact that schlieren imaging is sensitive to the index of refraction gradients. This point is displaced inwards from that at which the two components of the velocity vanish and is thus anticipated to correspond to a region of *upwelling* fluid. Direct flow visualization and wave-like excitations on the conduit edge that are advected upwards (Pesci *et al.* 2003; Dombrowski *et al.* 2005) indicate (*a*) that the edge is not a stagnation line and (*b*) that it is located within a region of upward flow.

A close-up of the region near the termination point of the moving wall is shown in figure 5(*g*) with streamlines superimposed. We see that the conduit edge is actually associated with the *separatrix* of the vortical flow driven by the wall. This is a crucial point, for it allows us to make connection with previous theoretical work on the structure of boundary layers between Rayleigh–Bénard convection cells (Shraiman 1987). To make this analogy precise, consider the schematic illustration in figure 7(*a*) of two adjacent convection cells bounded above and below by rigid walls held at

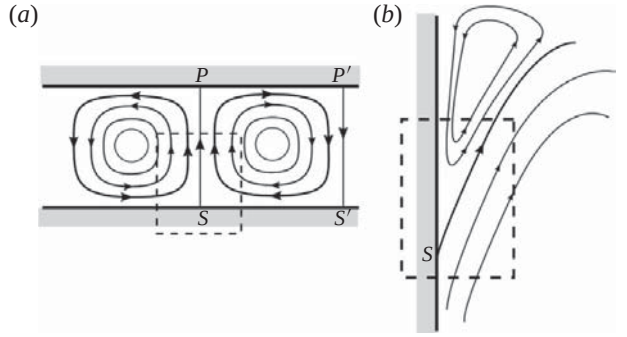

FIGURE 7. Vortices and separatrices in two flow geometries. (*a*) Convective rolls in Rayleigh–Bénard flow and (*b*) moving-wall-induced vortex.

different temperatures. The region near the bottom wall has a stagnation point $\mathscr{S}$ which marks the birth of the vertical separatrix which divides the two cells and also corresponds to the position of the boundary layer of the passive scalar. This phenomenon is also apparent in figure 3, where the peak gradient in $\hat{G}$ is clearly in the vicinity of $\xi \sim 75$, which is a region of upflow, since there is upflow for $\xi \lesssim 125$. A schematic of the flow in the moving-wall problem, shown in figure 7(*b*), reveals a similar topology, with the stagnation point $\mathscr{S}$ marking the birth of the separatrix between the vortical flows inside and outside of the conduit.

Given the above correspondence and the previous asymptotic analysis by Shraiman (1987), finding approximations to the separatrix location and velocity in its neighbourhood will suffice to explain the structure of the boundary layer at the conduit edge. We begin with the steady-state low-Reynolds-number version of (2.3),

$$\nu \nabla^2 \boldsymbol{u} = -g' \hat{\boldsymbol{k}}, \quad \kappa \nabla^2 g' = \boldsymbol{u} \cdot \nabla g' + N^2 w, \tag{4.3}$$

where, for this wall-driven flow, we have approximated the pressure by that of hydrostatic equilibrium with the background stratification. Close to the wall, horizontal velocities are negligible, and a parallel-flow approximation is valid. Near the conduit edge, where there are large lateral gradients in concentration, the full convective derivative must be taken into account. In the parallel-flow approximation, (4.3) reduces to

$$\nu \frac{\partial^2 w}{\partial x^2} = -g', \quad \kappa \frac{\partial^2 g'}{\partial x^2} = w \left(\frac{\partial g'}{\partial z} + N^2 \right), \tag{4.4}$$

which can be rendered dimensionless by the rescalings

$$\tilde{\xi} = \left(\frac{N}{\nu} \right)^{1/2} x, \quad \tilde{\zeta} = \frac{N}{W} z, \quad f = \frac{g'}{NW}, \quad \varpi = \frac{w}{W}, \tag{4.5}$$

where W is a characteristic velocity. Replacing into (4.4) we find

$$\frac{\partial^2 \varpi}{\partial \tilde{\xi}^2} = -f, \quad \epsilon \frac{\partial^2 f}{\partial \tilde{\xi}^2} = \varpi \left(\frac{\partial f}{\partial \tilde{\zeta}} + 1 \right), \tag{4.6}$$

where $\epsilon = \kappa/\nu = 1/Sc$. These equations can be combined into a single fourth-order partial differential equation (PDE),

$$\epsilon \frac{\partial^4 \varpi}{\partial \tilde{\xi}^4} - \varpi \frac{\partial^3 \varpi}{\partial \tilde{\zeta} \partial \tilde{\xi}^2} + \varpi = 0. \tag{4.7}$$

For $\epsilon \ll 1$ there are three regimes. (i) Far from the wall, when $\varpi \to 0$, the nonlinear term may be neglected, resulting in the linear fourth-order equation (Standing 1971) describing relaxation of the concentration field to the background density gradient. The characteristic scale of that decay is $\epsilon^{1/4}$. (ii) Near the wall, when $|\partial^4 \varpi / \partial \tilde{\xi}^4| \ll \epsilon^{-1}$, the first term may be neglected, and the solution of the resulting third-order equation describes the flow inside the conduit. (iii) In the intermediate boundary layer all the terms are equally important, and it is here that the parallel-flow approximation breaks down, and the neglected transverse velocity contribution must be considered.

In region (ii) we use lubrication theory and flux conservation to find the approximate location of the separatrix. Without loss of generality we assume that the moving wall terminates at $\tilde{\zeta} = 1$ and impose the boundary conditions on the velocity: $\varpi(0, \tilde{\zeta}) = 1 - \tilde{\zeta}$ and $\varpi(\tilde{h}(\tilde{\zeta}), \tilde{\zeta}) = 0$, where $\tilde{h}(\tilde{\zeta})$ is a function to be determined by imposing flux conservation. This yields the dimensional vertical velocity (for $0 < z \leqslant L$)

$$w(x, z) = \begin{cases} (N^2/6\nu) z\,(3x - h(z))\,(x - h(z)), & \text{if } x \leqslant h(z), \\ 0, & \text{if } x > h(z), \end{cases} \tag{4.8a}$$

where

$$h(z) = \left[\frac{6W\nu}{N^2} \frac{(1 - z/L)}{z} \right]^{1/2}. \tag{4.8b}$$

This functional form accurately captures the shape of the conduit as seen in figure 5, except as $z \to 0$ where, as expected, the assumptions of lubrication theory break down in the presence of a large lateral return flow to the wall.

Although the lubrication result is not a global solution of the kind necessary to find the separatrix exactly, we note from the numerical results that the separatrix lies close to the locus of maximum upward velocity w (figure 6*c*). In lubrication theory this maximum lies along the line $h_S(z) = (2/3)h(z)$. The horizontal velocity is found from continuity and by requiring that it changes sign at the separatrix such that it is positive inside the conduit and negative outside. We thus obtain the approximate velocity near the separatrix,

$$u(x, z) \simeq \frac{W}{3L} \left(\frac{2}{3} h(z) - x \right), \quad w(x, z) \simeq -\frac{W}{3} \left(1 - \frac{z}{L} \right), \tag{4.9}$$

where the overall negative sign on w indicates that this is an *upward* vertical velocity.

We analyse the concentration field near the separatrix, using the approximate velocity (4.9) by introducing rescaled variables centred at the boundary layer:

$$\chi = \frac{Pe^{1/2}}{\sqrt{3}L} \left(\frac{2}{3} h(z) - x \right), \quad \eta = \frac{Pe^{1/2}}{\sqrt{3}} \left(1 - \frac{z}{L} \right) \tag{4.10}$$

and $\phi = f - N^2 z$, where $Pe = WL/\kappa$ is the Péclet number. Retaining terms up to $O([W\nu Pe^{1/2}/L^3 N^2]^{1/2})$, the advection–diffusion equation (4.3) reduces to the PDE

$$\frac{\partial^2 \phi}{\partial \chi^2} + \chi \frac{\partial \phi}{\partial \chi} = -\frac{\partial^2 \phi}{\partial \eta^2} + \eta \frac{\partial \phi}{\partial \eta}. \tag{4.11}$$

The order considered corresponds to the condition $W/LN \ll (Re/Sc)^{1/4}$, which is well satisfied in the experiments. Equation (4.11) is identical to the PDE for the boundary layer straddling the separatrix in Rayleigh–Bénard convection, whose solution is obtained in terms of parabolic cylinder functions (Shraiman 1987, Appendix A). Translating those results shows that the concentration profile described by this

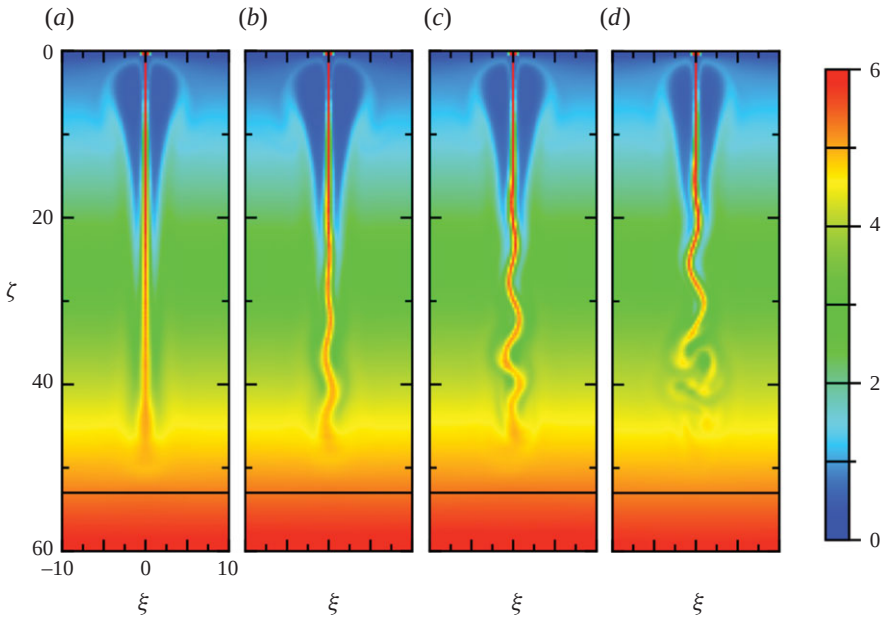

FIGURE 8. Development of the sinuous instability. Results for $Re_{in} = 0.05$, $Sc = 667$ and $Gr = 49.05$ for (a) the base flow and $\tau =$ (b) 133.67, (c) 200.33 and (d) 250.33. The horizontal black line marks the penetration depth for the equivalent base plume flow.

boundary layer interpolates between zero (corresponding to fresh water) inside the conduit and the local value of the stratification outside. These results show that the boundary layer width scales as $\delta \sim Pe^{-1/2}$ and in dimensional units is millimetric, thus offering an explanation for the sharpness of the gradient observed in the experiment.

5. Instability of the base flow plume

5.1. *Finite-amplitude behaviour*

We now consider a simulation with source conditions far beyond the instability threshold. Figure 8 shows the total reduced gravity $\hat{G}$ for the 'reference' flow, for the base (time-independent) flow and for three different times after the start of the calculation. Weak oscillations of the plume start from just under the recirculation zone at early times and grow, leading to the overturning of the filament. Although the instability is quite strong, the penetration depth differs little from that of the equivalent base plume flow.

Analysis of the rate of change of the kinetic energy sheds light on the development of this instability. Figure 9 shows the time evolution of the three terms in (2.13) at early times, and the inset shows the early-time evolution of the (normalized) kinetic energy density. For this simulation there is some evidence at very early times that the varicose instability grows, but it is rapidly convected away, and the later-time evolution is dominated by the sinuous instability. Both the boundary contributions and the transport terms play very small roles in the development of the perturbation and, as expected at very small Re, are overwhelmed by the viscous dissipation. Hence, the exponential growth is driven by the buoyancy forcing.

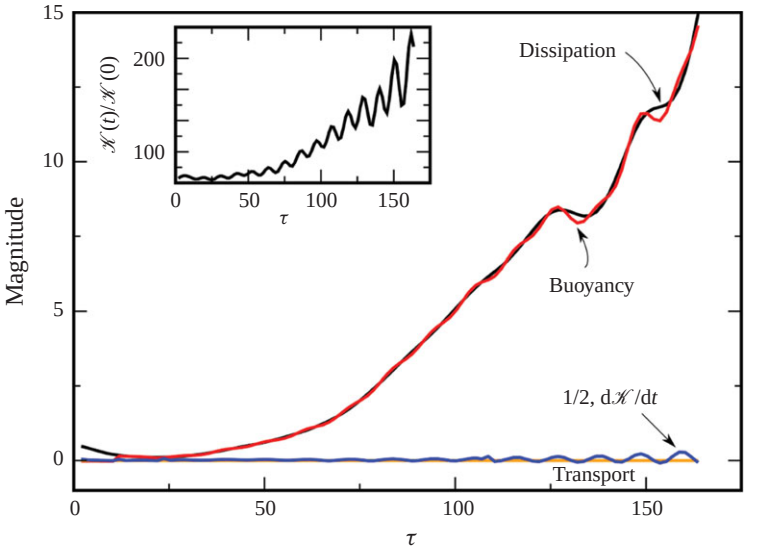

FIGURE 9. Energetics and growth of perturbations. The various contributions to power are shown as functions of time. The inset shows the temporal growth of the scaled perturbation kinetic energy.

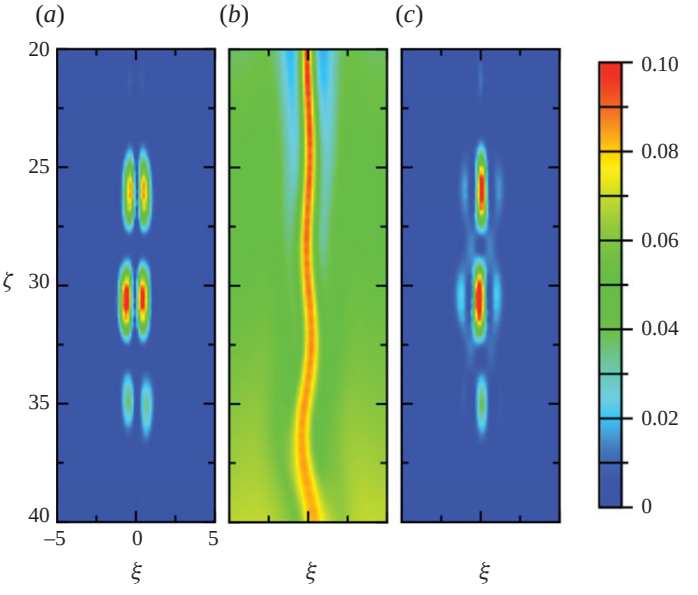

FIGURE 10. Spatial dependence of contributions to power balance for the sinuous instability. Localization of regions of (*a*) strong buoyancy flux contribution and (*c*) dissipation at time $\tau = 83.67$ compared with the total reduced gravity field $\hat{G}$ at time $\tau = 133.67$ shown in (*b*).

The global buoyancy and viscous dissipation contributions nearly cancel each other (figure 9). The spatial variation of the local perturbation buoyancy $\tilde{g}\tilde{w}$ and dissipation $\|\boldsymbol{\nabla}\tilde{\boldsymbol{u}}\|^2$ are shown in figure 10, and by comparison with the central panel (a close-up of figure 8*b*), it is clear that the buoyancy forcing is strongly correlated with generation of baroclinic vorticity. The latter is associated with large tilting of density isosurfaces at the base of the recirculation region. The strong forcing from the

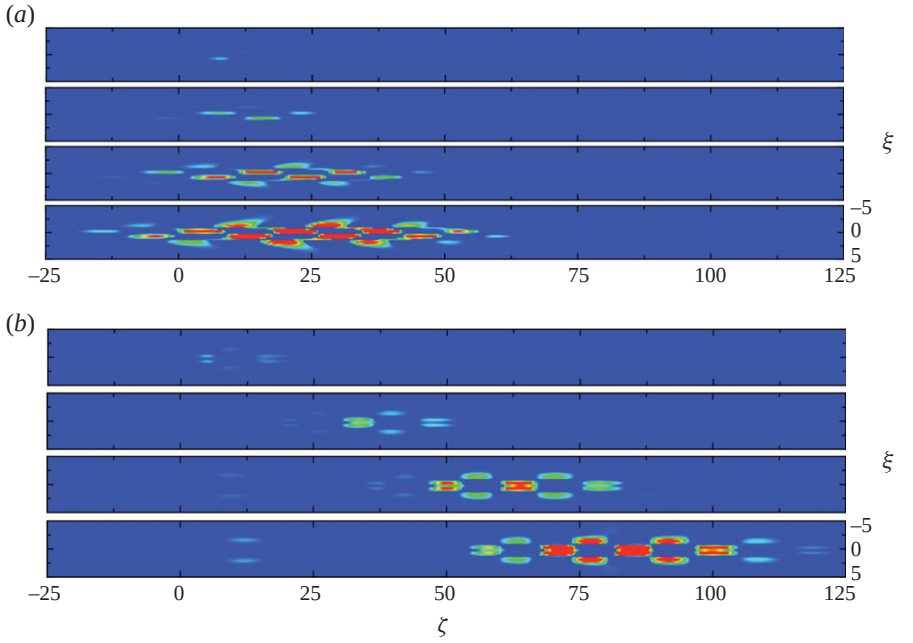

FIGURE 11. Plots of perturbation reduced gravity $\tilde{g}$ as defined in (2.10) for a 'reference case' linearized flow with the parameters as given in table 1 and $Re = 0.05$ in a parallel flow with vertical velocity and steady reduced gravity (g_s as in (2.10)) fields extracted from a base flow plume at height $\zeta_S = 16$ for times $\tau = 13.33$, 46.67, 80 and 106.67 after the initial perturbation for (a) sinuous and (b) varicose perturbations.

density field is inherently related to the low solute diffusivity, which allows very large horizontal gradients in density and thus significant baroclinic torques. In contrast, the dissipation is dominated by the term $(\partial\hat{w}/\partial\xi)^2$, which peaks in the interiors of the vortical domains.

5.2. *Onset of the global instability*

We computed base flow plumes for various Re values and perturbed them with both sinuous perturbations and low-amplitude noise. Tracking the kinetic energy, we found that perturbations grow for $Re \gtrsim 0.02$, with dynamics qualitatively similar to the ones above. The local stability properties of the base flows were obtained for various Re values and with $Gr = 49.05$ and $\sigma = 667$ by examining $w_S^\zeta(\xi)$ and $g_S^\zeta(\xi)$ at selected depths ζ_S, as described in § 2.3. The chosen depths ζ_S range from the base of the recirculation region to near the end of the plume. No profile was taken inside the recirculation region because the horizontal velocity $u_s(\xi, \zeta_S)$ there is not negligible, violating the parallel-flow assumption. These approximately parallel flows were perturbed at $\tau = 0$ with an asymmetric impulse-like initial condition of small amplitude. We then decompose the fields into their sinuous and varicose parts. For varicose perturbations the horizontal speed $\tilde{u}$ is antisymmetric, while the vertical speed $\tilde{w}$ and the perturbation reduced gravity $\tilde{g}$ are symmetric; the sinuous perturbations have opposite symmetries.

We focus first on the qualitative aspects of the reduced gravity field. For the sinuous instability, we plot $\hat{g}$ in figure 11(a) for the case $Re = 0.05$, well into the absolutely unstable regime. The initial localized perturbation was introduced at $\zeta_0 = 0$, and the parallel profiles $w_S(\xi, \zeta_S)$ and $g_S(\xi, \zeta_S)$ (as defined in (2.15)) were

computed at $\zeta_S = 16$, i.e. just below the recirculation region. The perturbation clearly grows in time downstream, and the signal also propagates slightly upstream. The sinuous perturbation has alternating areas of high positive and negative values, arranged symmetrically with respect to the central axis, since the perturbation reduced gravity tracks the plume shape. That is, when the plume bends to the right, the left perturbation reduced gravity is negative. Similarly, the conduit region on the left increases in density because of the bending of the conduit. This explanation is analogous to that given by Lister (1987) for an instability due to a different physical mechanism. The horizontal velocity field (not shown) has a similar structure, while the vertical velocity field is antisymmetric. Clearly, this corresponds to an absolute instability, and as is apparent in figure 8(*d*), although the perturbation indeed grows downstream, it also extends all the way up to the edge of the recirculation region.

Turning to the varicose instability, figure 11(*b*) shows $\tilde{g}$ for the reference flow at $Re = 0.05$. The perturbation field is an alternating distribution of positive and negative values, associated with dilation and constriction of the plume. As with all unstable source conditions considered, the growing perturbation is convected downstream. Yet, with such a relatively large value of Re, absolute instability is incipient for a second branch of nearly neutral modes. Once the sinuous instability appears it rapidly dominates the varicose mode, and it is difficult to determine if the latter is strictly convectively unstable. However, the parallel profile analysis is fully consistent with a convective varicose mode.

Similar impulse responses have been computed for three characteristic flows obtained with $Gr = 49.05$, $Sc = 667$ and respectively $Re = 0.01$ (found to be a globally stable case), $Re = 0.02$ (weakly globally unstable, quite close to a marginal case) and $Re = 0.03$ (globally unstable) for which the total easily identifiable length of the plume is typically of the order of $\zeta \sim 40$, and the end of the recirculation region is located at a distance of approximately $\zeta \sim 12$ from the source. The methods described in § 2 have been applied to these impulse responses computed at selected stations ζ_S to determine the spatio-temporal stability nature of the local flow. A typical example is given by the analysis of the profile at $\zeta_S = 18$ below the source for $Re = 0.03$ which is slightly above the threshold for the onset of the global instability. Figure 12 shows the temporal evolution of the amplitude, obtained by Hilbert transform, of the perturbation reduced gravity for both the (*a*) sinuous and (*b*) varicose parts of the signal. We observe that both amplitudes increase in time, implying that both kinds of perturbations are unstable. Since the amplitude of the sinuous mode clearly grows at the initial pulse position $\zeta = \zeta_0$, the mode is absolutely unstable. On the other hand, the very small amplitude of the varicose signal at $\zeta = \zeta_0$, comparable to the numerical roundoff noise, prevents an unambiguous determination of the character of the instability that however appears to be convectively unstable or, at worst, at the inception of absolute instability (there is no clear growth of the signal in $\zeta = \zeta_0$). These conclusions are further supported by replotting the amplitudes as a function of $v_g = (\zeta - \zeta_0)/\tau$ for increasing times (figure 12*c*). Here again it is seen how sinuous modes with zero group velocity increase their amplitude, while the corresponding varicose modes remain of smaller amplitude. This is confirmed by the computation of the associated spatio-temporal growth rates σ, plotted in figure 12(*d*). The absolute growth rate $\sigma(v_g = 0)$ of sinuous perturbations is clearly positive. Similar results are obtained by post-processing the $\tilde{u}$ and $\tilde{w}$ velocity fields.

Similar analyses at other selected streamwise stations show that the appearance of the sinuous instability follows the classical scenario in which a sufficiently large region of amplified local absolute instability precedes the onset of the global mode.

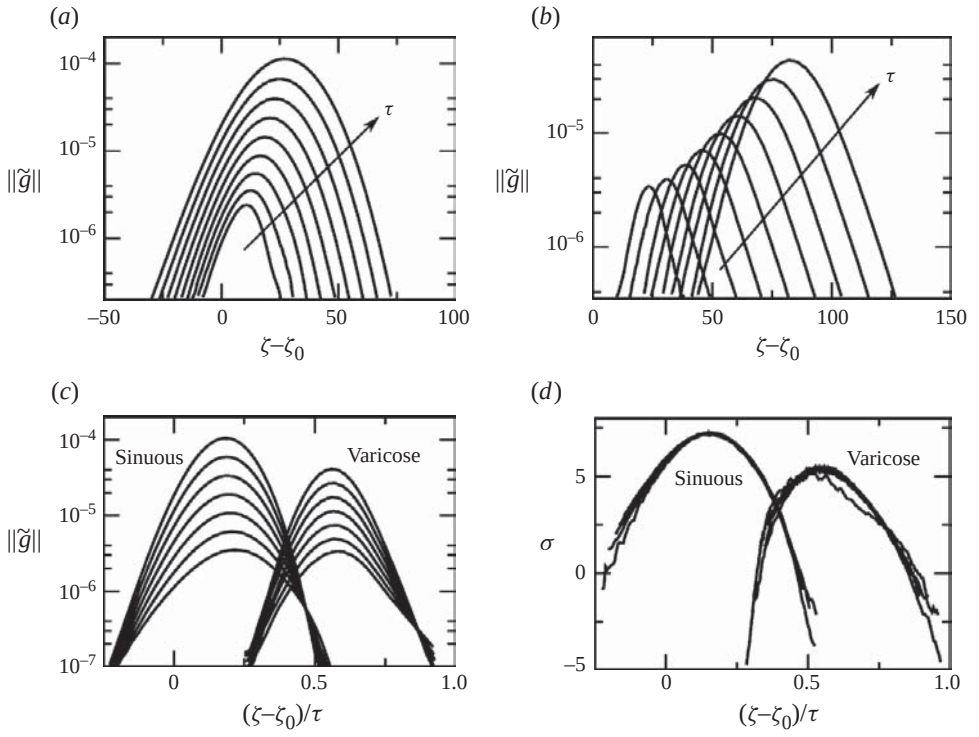

FIGURE 12. Amplitude of the perturbation reduced gravity $\tilde{g}$ versus the spatial coordinate $\zeta - \zeta_0$ for times from $\tau = 40$ to $\tau = 146.67$ with time interval 13.33, for a flow with parallel-flow profiles extracted at $\zeta_S = -18$, corresponding to somewhat less than half the total length of the plume for $Re = 0.03$ for (a) sinuous and (b) varicose perturbations. (c) Amplitude and (d) growth rate σ of the perturbation reduced gravity $\tilde{g}$ versus the group velocity v_g on the ray $v_g = (\zeta - \zeta_0)/\tau$ for times from $\tau = 66.67$ to $\tau = 146.67$ with time interval 13.33.

Because such a region of absolute instability does not occur for the parameter values studied here, varicose perturbations, even if locally unstable, do not give birth to a global mode.

6. Conclusions

This work was motivated by the experiments (Pesci *et al.* 2003) in which a salty plume penetrating a stratified environment in a Hele-Shaw cell becomes unstable and oscillates when the injected flux exceeds a critical value. Here, we studied laminar plumes in a two-dimensional stratified environment through DNS, scaling analyses and simplified analytical models. These approaches capture fully the main experimental observations and lead to the identification of the key physical mechanisms at work. A base flow plume has been found for all source conditions, and the dominant scalings with the flow parameters have been identified. In particular, the penetration depth has been shown to be a characteristic of this base flow plume, and not a consequence of the instability, for it is determined by the rapid diffusion of the density in the vicinity of the recirculation region and to a lesser extent by diffusion from the conduit. These are the two parts of the flow identified by Pesci *et al.* (2003) and analysed asymptotically here.

The dominant sinuous instability observed at sufficiently high flow rates is forced mainly by the horizontal density gradient. These gradients, whose existence depends crucially on the high Schmidt number, lead to strong generation of baroclinic vorticity, which ultimately drives the flow. A local stability analysis shows that the sinuous instability, following the classical scenario of global mode destabilization (Huerre 2001; Chomaz 2005), is strongly absolutely unstable in a finite spatial region at the onset of the global mode instability. This behaviour is analogous to that of the flickering candle that was proposed by Maxworthy (1999), although the physical growth mechanisms would appear to be different. The subdominant varicose modes do not display such features and thus do not lead to any self-sustained varicose oscillations. It is noteworthy that the buoyancy force can lead to the development of what is essentially an inertial instability at very small Reynolds numbers because of the baroclinic torques.

While the two-dimensional model studied here is a suitable approximation to Hele-Shaw dynamics, more recent experiments (Dombrowski *et al.* 2005) on three-dimensional jets found phenomena which may not be realized in such a model. These include a helical jet instability with a braided recirculating flow and a distance-dependent synchronization between neighbouring jets. The microscopic origin of the synchronization and whether this last phenomenon also exists in two dimensions remain as open questions.

We thank H. K. Moffatt and N. O. Weiss for discussions. This work was supported in part by the EU Marie Curie International Reintegration Grant MIRG-CT-2005-016563 (M.L. and C.P.C.), a French Government Fellowship at Churchill College (C.C.), the Schlumberger Chair Fund and the BP Institute.

REFERENCES

Auteri, F., Guermond, J.-L. & Parolini, N. 2001 Role of the LBB condition in weak spectral projection methods. *J. Comput. Phys.* **174**, 405–420.

Batchelor, G. K. 1954 Heat convection and buoyancy effects in fluids. *Q. J. R. Meteorol. Soc.* **80**, 339–358.

Blanchette, F., Peacock, T. & Cousin, R. 2008 Stability of a stratified fluid with a vertically moving sidewall. *J. Fluid Mech.* **609**, 305–317.

Brandt, L., Cossu, C., Chomaz, J.-M., Huerre, P. & Henningson, D. S. 2003 On the convectively unstable nature of optimal streaks in boundary layers. *J. Fluid Mech.* **485**, 221–242.

Cartwright, J. H. E., Garcia-Ruíz, J. M., Novella, M. L. & Otálora, F. 2002 Formation of chemical gardens. *J. Colloid Interface Sci.* **256**, 351–359.

Chomaz, J.-M. 2005 Global instabilities in spatially developing flows: non-normality and nonlinearity. *Annu. Rev. Fluid Mech.* **37**, 357–392.

Davis, T. A. & Duff, I. S. 1997 An unsymmetric-pattern multifrontal method for sparse LU factorization. *SIAM J. Matrix Anal. Appl.* **18**, 140–158.

Delbende, I. & Chomaz, J.-M. 1998 Nonlinear convective/absolute instabilities of parallel two-dimensional wakes. *Phys. Fluids* **10**, 2724–2736.

Delbende, I., Chomaz, J.-M. & Huerre, P. 1998 Absolute/convective instabilities in the Batchelor vortex: a numerical study of the linear impulse response. *J. Fluid Mech.* **355**, 229–254.

Dombrowski, C., Lewellyn, B., Pesci, A. I., Restrepo, J. M., Kessler, J. O. & Goldstein, R. E. 2005 Coiling, entrainment, and hydrodynamic coupling of decelerated fluid jets. *Phys. Rev. Lett.* **95**, 184501.

Drazin, P. G. & Riley, N. 2006 *The Navier–Stokes Equations: A Classification of Flows and Exact Solutions.* Cambridge University Press.

Helfrich, K. R. & Whitehead, J. A. 1990 Solitary waves on conduits of buoyant fluid in a more viscous fluid. *Geophys. Astrophys. Fluid Dyn.* **51**, 35–52.

Hill, R. I., Campbell, I. H., Davies, G. F. & Griffiths, R. W. 1992 Mantle plumes and continental tectonics. *Science* **256**, 186–193.

Huerre, P. 2001 Open shear flow instabilities. In *Perspectives in Fluid Dynamics* (ed. G. K. Batchelor, H. K. Moffatt & M. G. Worster), pp. 159–229. Cambridge University Press.

Katz, R. F. & Worster, M. G. 2008 Simulation of directional solidification, thermochemical convection, and chimney formation in a Hele-Shaw cell. *J. Comput. Phys.* **227**, 9823–9840.

Kessler, J. O. 1985 Hydrodynamic focusing of motile algal cells. *Nature* **313**, 218–220.

Kessler, J. O. 1986 Individual and collective fluid-dynamics of swimming cells. *J. Fluid Mech.* **173**, 191–205.

Lister, J. R. 1987 Long-wavelength instability of a line plume. *J. Fluid Mech.* **175**, 413–428.

Lombardi, M. 2008 Numerical analysis of a laminar plume in a stratified environment. MPhil thesis, BP Institute, University of Cambridge, Cambridge, UK.

Maxworthy, T. 1999 The flickering candle: transition to a global oscillation in a thermal plume. *J. Fluid Mech.* **390**, 297–323.

Moffatt, H. K. 1978 *Magnetic Field Generation in Electrically Conducting Fluids*. Cambridge University Press.

Morton, B. R., Taylor, G. & Turner, J. S. 1956 Turbulent gravitational convection from maintained and instantaneous sources. *Proc. R. Soc.* A **234**, 1–23.

Peppin, S. S. L., Huppert, H. E. & Worster, M. G. 2008 Steady-state solidification of aqueous ammonium chloride *J. Fluid Mech.* **599**, 465–476.

Pesci, A. I., Porter, M. A. & Goldstein, R. E. 2003 Inertially driven buckling and overturning of jets in a Hele-Shaw cell. *Phys. Rev.* E **68**, 056305.

Rhines, P. B. & Young, W. R. 1983 How rapidly is a passive scalar mixed within closed streamlines. *J. Fluid Mech.* **133**, 133–145.

Ribe, N. M. 2004 Coiling of viscous jets. *Proc. R. Soc.* A **460**, 3223–3239.

Schofield, S. P. & Restrepo, J. M. 2010 Stability of planar buoyant jets in stratified fluids. *Phys. Fluids* **22**, 053602.

Shraiman, B. I. 1987 Diffusive transport in a Rayleigh–Bénard convection cell. *Phys. Rev.* A **36**, 261–267.

Standing, R. G. 1971 The Rayleigh problem for a slightly diffusive density-stratified fluid. *J. Fluid Mech.* **48**, 673–688.

Stone, D. A. & Goldstein, R. E. 2004 Tubular precipitation and redox gradients on a bubbling template. *Proc. Natl Acad. Sci. USA* **101**, 11537–11541.

Stone, D. A., Lewellyn, B., Baygents, J. C. & Goldstein, R. E. 2005 Precipitative growth templated by a fluid jet. *Langmuir* **21**, 10916–10919.

Thouvenel-Romans, S. & Steinbock, O. 2003 Oscillatory growth of silica tubes in chemical gardens. *J. Am. Chem. Soc.* **125**, 4338–4341.

Thouvenel-Romans, S., van Saarloos, W. & Steinbock, O. 2004 Silica tubes in chemical gardens: radius selection and its hydrodynamic origin. *Europhys. Lett.* **67**, 42–48.

Weiss, N. O. 1966 The expulsion of magnetic flux by eddies *Proc. R. Soc. Lond.* A **293**, 310–328.

Weissburg, M. J. & Zimmer-Faust, R. K. 1994 Odor plumes and how blue crabs use them in finding prey. *J. Exp. Biol.* **197**, 349–375.